

The Orbital Geometries and Stellar Obliquities of Exoplanet-Hosting Multi-Star Systems

MALENA RICE,¹ KONSTANTIN GERBIG,¹ AND ANDREW VANDERBURG²

¹*Department of Astronomy, Yale University, New Haven, CT 06511, USA*

²*Department of Physics and Kavli Institute for Astrophysics and Space Research, Massachusetts Institute of Technology, Cambridge, MA 02139, USA*

ABSTRACT

The current orbital geometries of exoplanet systems offer a fossilized record of the systems' dynamical histories. A particularly rich set of dynamical mechanisms is available to exoplanets residing in multi-star systems, which may have their evolution shaped by the gravitational influence of bound stellar companions. In this work, we examine the joint distribution of stellar obliquities and orbital orientations for transiting exoplanets residing within astrometrically resolved binary and triple-star systems. We leverage existing constraints on stellar obliquities in exoplanet systems, together with astrometric measurements from *Gaia* DR3, to uncover a set of fully-aligned, “orderly” exoplanet systems that exhibit evidence of both spin-orbit and orbit-orbit alignment. We also find evidence that the observed distribution of orbit-orbit orientations in our sample is more strongly peaked toward alignment than an isotropic distribution. Our results may be indicative of efficient viscous dissipation by nodally recessing protoplanetary disks, demonstrating a regime in which stellar companions produce and maintain order in planetary systems, rather than enhancing misalignments.

Keywords: planetary alignment (1243), exoplanet dynamics (490), star-planet interactions (2177), exoplanets (498), binary stars (154), exoplanet systems (484)

1. INTRODUCTION

A significant subset of all known exoplanet systems include a host star with one or more bound stellar companions (e.g. Matson et al. 2018; Fontanive & Bardalez Gagliuffi 2021). These N -body systems can span a tremendous range of relative spin-orbit and orbit-orbit configurations, offering rich insights into the processes of star and planet formation. The geometries of these complex systems may reflect and inform the initial conditions within systems' natal molecular clouds (Bate 2000; Bate et al. 2010; Spalding et al. 2014), as well as long-term secular interactions with stellar companions (e.g. Naoz et al. 2012; Batygin 2012; Lai 2014; Naoz 2016).

Exoplanet spin-orbit angles, which serve as a proxy for stellar obliquities in exoplanet-hosting systems, provide an important lens into systems' dynamical histories. Spin-orbit angles can be measured using a range of methods reviewed in Albrecht et al. (2022), with the most widespread methods being the Rossiter-McLaughlin effect (Rossiter 1924; McLaughlin 1924),

Doppler tomography (e.g. Collier Cameron et al. 2010; Gandolfi et al. 2012), and starspot crossing events (e.g. Sanchis-Ojeda & Winn 2011; Dai et al. 2017). Each of these methods offers an avenue to constrain the sky-projected spin-orbit angle, λ , of a transiting exoplanet. Several past and ongoing surveys have collected spin-orbit measurements over recent decades (e.g. Queloz et al. 2000; Albrecht et al. 2011a; Albrecht et al. 2012; Rice et al. 2021), leading to the discovery of many heavily spin-orbit misaligned exoplanets (Albrecht et al. 2021) and culminating in a collection of spin-orbit measurements currently tracked within the TEPcat catalogue (Southworth 2011).

The orbital orientations of multi-star systems reveal architectural insights that are complementary to those of spin-orbit orientations. Stellar binary and triple orbital orientations can be constrained through astrometric parallaxes and proper motion measurements (e.g. Pearce et al. 2020; Tokovinin 2020, 2022). Using the *Gaia* DR3 (Gaia Collaboration et al. 2016, 2022) catalogue of high-precision stellar astrometry, it is now possible to derive sky-projected stellar orbital orientations with substantially improved precision.

In this paper, we examine the joint distributions of spin-orbit and orbit-orbit orientations in multi-star sys-

tems hosting at least one transiting exoplanet. The work presented here is motivated by the recent finding that, at a population level, moderately wide binary systems that host transiting exoplanets are more often edge-on than field binaries, indicating a tendency toward orbit-orbit alignment in these systems (Christian et al. 2022; Dupuy et al. 2022). Here, we add a new, complementary facet to this picture: the role of spin-orbit alignment in binary systems.

We first demonstrate the existence of a population of “orderly”, fully aligned systems that exhibit evidence of both spin-orbit and orbit-orbit alignment. We also find that the full distribution of orbit-orbit inclinations is more strongly peaked than an isotropic distribution, with a joint overabundance of aligned systems and dearth of orthogonal relative orbital orientations.

Primordial orbit-orbit alignment may naturally arise in multi-star systems that form through disk fragmentation – a mechanism in which one or more stellar companions are born from a gravitationally unstable circumprimary disk that inherits the primary’s angular momentum vector (Adams et al. 1989; Bonnell & Bate 1994). This mechanism may help to explain the orbit-orbit aligned configurations observed for some shorter-period binary and multi-star systems (e.g. Zhang et al. 2023; Lester et al. 2023). However, the separations at which disk fragmentation can occur are bounded by the extent of the circumprimary disk. Disk fragmentation is, accordingly, expected to operate at relatively small companion separations $a \lesssim 200$ au (Krumholz et al. 2007; Tobin et al. 2016), whereas the population probed in this work is dominated by moderate- to wide-separation systems.

As a result, we instead suggest that these observations provide evidence for efficient viscous dissipation during the protoplanetary disk phase, pushing systems toward orbit-orbit alignment while star-disk gravitational coupling maintains spin-orbit alignment. Our findings offer an observational counterpart to pre-existing theoretical frameworks that examine the influence of viscous dissipation on binary system alignment (Bate et al. 2000; Lubow & Ogilvie 2000; Foucart & Lai 2014; Zanazzi & Lai 2018).

Previous work has examined the range of available mechanisms through which stellar companions can excite the observed set of spin-orbit misalignments in exoplanet systems (e.g. Naoz et al. 2012; Batygin 2012; Vick et al. 2023). By contrast, we identify and examine a regime of observed exoplanet systems in which stellar companions are more likely to have enhanced *order* by pushing systems toward alignment.

2. METHODS

2.1. Initial sample selection

We began by downloading the catalogue of all exoplanet spin-orbit angle measurements from TEPcat (Southworth 2011) on 12/30/2022. This catalogue, which includes a comprehensive, up-to-date listing of all published spin-orbit measurements, included 307 spin-orbit measurements obtained for 186 planets. Where multiple measurements were available for a given planet, the following criteria were applied to select a single measurement for our sample:

- More recent publications that incorporated both new and previous data were favored.
- To maximize the uniformity of our sample, measurements made using either the Rossiter-McLaughlin effect or Doppler tomography were generally favored over spot-crossing measurements.
- For measurements that leveraged the Rossiter-McLaughlin effect, observations with full transit coverage – and particularly those with pre- and post-transit baseline observations – were favored.
- Measurements with no clear structure remaining in the Rossiter-McLaughlin residuals were favored.

Kepler-408 b was excluded from our sample because it has only a measured inclination, with no λ measurement available (Kamiaka et al. 2019). We also removed WASP-2 b from our sample because of its contested stellar obliquity measurement (Triaud et al. 2010; Albrecht et al. 2011b). In total, this left 184 individual planets¹ each with a sky-projected spin-orbit angle measurement.

2.2. Collating sample properties

We then cross-matched these 184 planets with the NASA Exoplanet Archive’s Planetary Systems Composite Parameters table (PSCompPars; NASA Exoplanet Archive 2023) to extract host star properties and coordinates, as well as planetary properties other than λ . Six of the 184 planets were not found in the PSCompPars table: TOI-778 b, TOI-1937 b, WASP-30 b, WASP-109 b, WASP-111 b, and WASP-134 b. For these planets,

¹ WASP-30 b has a sufficiently high mass ($M = 60.86 \pm 0.89 M_J$) such that it may be more appropriately classified as a brown dwarf, rather than a planet (Anderson et al. 2011a). Nevertheless, we retained the system within our sample at this stage for completeness. No stellar companions were found for WASP-30 in Section 2.3, such that this system was not included in the bulk of our analysis.

system properties were instead drawn from the Extrasolar Planet Encyclopaedia.²

Next, we cross-matched these systems with sources within the *Gaia* DR3 catalogue using the RA, Dec (α , δ) coordinates of each host star and a search radius of $5''$. From this search, we obtained a single match to each of 149 sources, two matches to each of 32 sources, and three matches to each of 3 sources. For systems with a single match, we adopted that *Gaia* DR3 source as the host star. For systems with two or three matches, we cross-verified the host star’s magnitude with candidate sources’ stellar magnitudes to match the appropriate source to the host star of interest.

2.3. Characterizing stellar multiplicity

Once the planet-hosting sources were identified in *Gaia* DR3, we carried out a series of tests to identify bound stellar companions. In this way, we developed a robustly vetted sample of binary and triple-star systems for further study. No systems were found with more than three identified stellar components.

First, we conducted a cone search with radius $10'$ around each host star to search for bound stellar companions. We followed the methods of El-Badry et al. (2021) to vet candidate companion sources (see Section 5.1 of Rice et al. (2023) for a detailed overview of our vetting process). From this initial vetting step, we identified 44 host stars within our sample that reside in a system with at least one astrometrically observed stellar companion, including 43 tentative binary star systems and one triple-star system.

We cross-validated our identified systems with the binary catalogue derived in El-Badry et al. (2021) and found that all 43 of our identified binary systems were also recovered within their study. All 43 identified pairs also have a low chance alignment probability $R < 0.02$ as derived in El-Badry et al. (2021), with most systems having $R < 1 \times 10^{-4}$.

Our initial vetting process excluded some host stars within our full sample that had both (1) a spin-orbit constraint and (2) one or more previously identified stellar companions that did not pass our tests. Through a literature search and cross-match with the NASA Exoplanet Archive, we identified 22 candidate multi-star systems in our sample, including 19 candidate binary star systems and three candidate triple-star systems, that had no bound companions identified by our first vetting step. We also found that three of our initially identified binary candidates (K2-290, Kepler-13, and WASP-24) are

instead likely triple-star systems (Hjorth et al. 2019; Murgauer 2019).

To investigate whether any of the 22 candidate multi-star systems could be included within our final sample, we examined the systems’ astrometric fits, projected separations, and stellar magnitudes. The Renormalized Unit Weight Error (RUWE) parameter reported by *Gaia* DR3 is a metric used to quantify how well a single-star model fits to the astrometric observations of a given source, where $\text{RUWE} \sim 1.0$ signifies a good fit. Five of the 19 candidate binary systems (KOI-1257, WASP-2, WASP-20, WASP-72, and WASP-76) have primary stars with $\text{RUWE} > 1.4$, suggesting that their stellar companions may be blended with the primary source and unresolvable with *Gaia* astrometry. For another six candidate binary systems (TrES-2, HAT-P-14, HAT-P-27, HAT-P-29, HAT-P-32, and WASP-3) and two triple-star systems (HAT-P-8 and WASP-12), all stellar companions are relatively faint and located within $\sim 0.5\text{--}4''$ of the primary, such that they are likely also unresolved by *Gaia* (Wöllert & Brandner 2015; Ngo et al. 2015; Belokurov et al. 2020; Dupuy et al. 2022). These systems with no astrometrically constrained secondary sources could not be reincorporated into our final sample.

Five of the remaining systems (55 Cnc, HAT-P-20, EPIC 246851721, Kepler-89, and WASP-180) were recovered by loosening our parallax constraint, such that systems with relatively wide-separation (projected angular separation $\theta_s > 4.0''$) companion candidates were accepted into the sample with parallaxes consistent up to 6σ (compared with our initial 3σ requirement adopted from El-Badry et al. (2021)). One candidate triple-star system (WASP-11)³ and two candidate binary star systems (WASP-1 and WASP-33) were recovered by loosening our proper motion constraint, such that systems with relative proper motions consistent up to 5σ were accepted into the sample (compared with our initial 2σ requirement). This loosened proper motion constraint also recovered an additional binary system candidate – HAT-P-70 – which has not been previously flagged as a binary system in past publications.

While a visual binary stellar companion to WASP-31 was previously identified at a relatively wide separation of $35''$ (Anderson et al. 2011b), we recovered no companion candidates that fit our looser constraints. WASP-31 has $\text{RUWE}=0.99$ and was not identified by El-Badry et al. (2021) as a component of a stellar binary sys-

² <http://exoplanet.eu/>

³ Only one stellar companion to WASP-11 was recovered within *Gaia* DR3. However, WASP-11 has $\text{RUWE}=3.60$, indicating that the more nearby of its two stellar companions is likely unresolved.

tem. We also rule out the possibility that the binary star could have moved directly behind the primary during the time span between its initial detection and its observation by *Gaia*, since a $35''$ separation corresponds to a projected distance of $\sim 13,600$ au for a parallax $\varpi = 2.5757$ mas from *Gaia* DR3. We conclude that the previously identified visual binary companion was likely a chance alignment, rather than a bound companion.

In total, therefore, we recovered three initial binary candidates that were moved into our triple-star sample, eight additional candidate binary systems, and one additional candidate triple-star system. As expected based on our adopted constraints, none of the newly incorporated binary systems were listed within the binary star catalog developed by El-Badry et al. (2021).

The systems that were not accepted into the sample using our original constraints are included in our “loose” sample, while they are excluded from our “strict” sample. Our “loose” sample includes 48 binary star systems and 5 triple-star systems, while our “strict” sample includes 40 binary star systems and 4 triple-star systems. The remainder of this work focuses on the more conservative “strict” sample in which all systems have passed our full vetting analysis. For thoroughness, we also consider the “loose” sample as a comparison point in Section 3.2. All systems in each sample include a transiting planet with a spin-orbit measurement orbiting the primary star, as well as astrometric constraints from *Gaia* DR3 for both the primary, planet-hosting star and at least one stellar companion.

2.4. Astrometric orbital constraints

We next constrained the distribution of sky-projected stellar orbit configurations in our sample based on precise position and proper motion measurements from *Gaia* DR3. Taken jointly with the existing set of exoplanet spin-orbit measurements, the relative stellar position and velocity vectors in multi-star systems can inform the range of full system geometries. Some potential configurations for exoplanet-hosting binary star systems are demonstrated in Figure 1 for reference.

Using *Gaia* DR3, we extracted the relative sky-projected position and velocity vectors \vec{r} and \vec{v} of the two stars within each binary system. The angle γ between these two vectors is defined as

$$\cos \gamma = \frac{\vec{r} \cdot \vec{v}}{|\vec{r}| |\vec{v}|} \quad (1)$$

where

$$\vec{r} \equiv [\Delta\alpha, \Delta\delta] \quad (2)$$

and

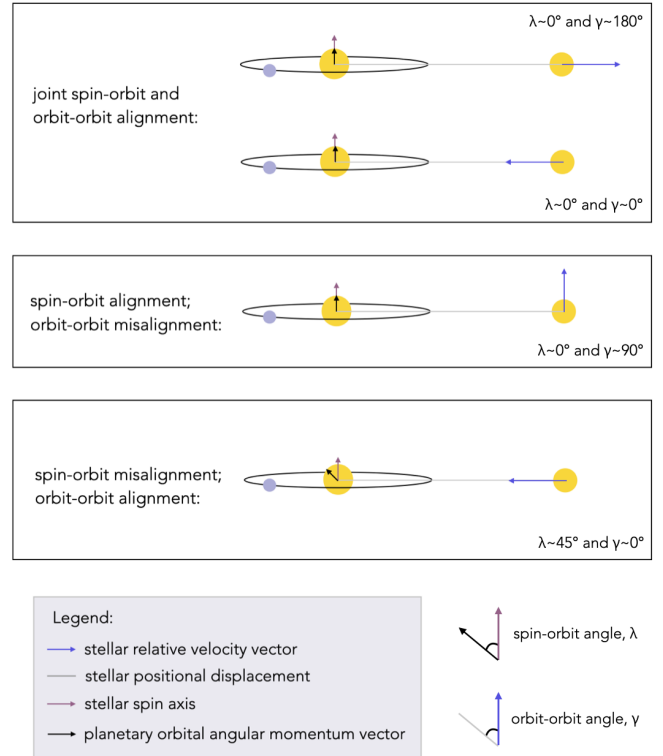


Figure 1. A selection of potential spin-orbit and orbit-orbit configurations for binary star systems with a circumpriary, transiting exoplanet. The transiting planet’s orbit is shown in these example systems, while only the relative positional displacement and velocity vector are displayed for the stellar binary orbit.

$$\vec{v} \equiv [\Delta\mu_\alpha^*, \Delta\mu_\delta]. \quad (3)$$

Here, $\Delta\alpha$ and $\Delta\delta$ are the positional differences between the primary and companion position in the RA and Dec directions, respectively, while $\Delta\mu_\alpha^*$ and $\Delta\mu_\delta$ are the corresponding proper motion differences in the RA and Dec directions. We note that *Gaia* DR3 reports proper motions μ_α^* that have already incorporated a $\cos \delta$ corrective factor in the RA direction, such that $\mu_\alpha^* \equiv \mu_\alpha \cos \delta$.⁴

The angle γ has been previously used to characterize the eccentricity distribution of wide stellar binary systems (Tokovinin & Kiyaveva 2015). Two well-defined cases for γ in binary star systems – shown for edge-on orbits ($\gamma \sim 0^\circ$ or $\gamma \sim 180^\circ$) and for face-on, circular orbits ($\gamma \sim 90^\circ$) – are demonstrated in Figure 2 for

⁴ See the pmra definition in the *Gaia* DR3 source documentation at https://gea.esac.esa.int/archive/documentation/GDR3/Gaia_archive/chap_datamodel/sec_dm_main_source_catalogue/ssec_dm_gaia_source.html.

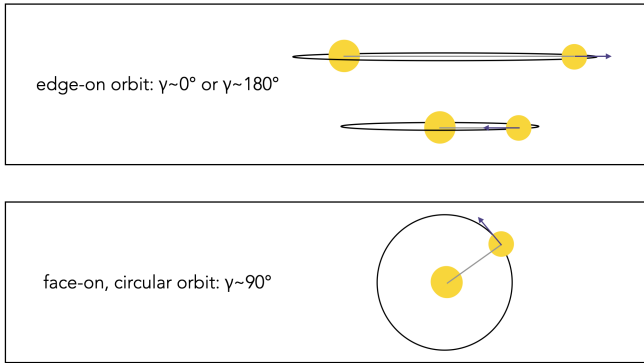


Figure 2. Two well-defined cases for γ : edge-on orbits ($\gamma \sim 0^\circ$ or $\gamma \sim 180^\circ$) and circular, face-on orbits ($\gamma \sim 90^\circ$). Here, the stellar binary orbit is shown for reference. Edge-on orbits always remain close to $\gamma \sim 0^\circ$ or $\gamma \sim 180^\circ$, whereas face-on orbits span a wide range of γ values for nonzero eccentricities. The stellar relative velocity vector and positional displacement are colored here as in Figure 1.

reference. Systems with eccentric and/or moderately inclined orbits generally lie between these two extremes.

To derive our adopted γ values and associated uncertainties, for each system we drew 30,000 random samples of each input variable – α , δ , μ_α^* , and μ_δ for both the primary and secondary star – from *Gaia* DR3. Parameter covariances were accounted for by multiplying the Cholesky decomposition of the correlation matrix describing these four variables with a normalized vector of uncorrelated Gaussian random variables. For most systems, this sampling produced a roughly Gaussian distribution of γ values that was used to derive a new mean (adopted as γ) and standard deviation (σ_γ).

The sampling for a few systems with $\gamma \sim 0^\circ$ or $\gamma \sim 180^\circ$ suffered from clear edge effects imposed by the definition of γ , which must exist within the range $0^\circ \leq \gamma \leq 180^\circ$. For these systems, the sampled distribution emerged as a truncated Gaussian. In such cases, we found the peak of the Gaussian using a 100-bin histogram, and we mirrored the histogram across its central point before deriving γ and σ_γ . The new, mirrored histogram allowed for values $\gamma < 0^\circ$ and $\gamma > 180^\circ$ for the purpose of deriving appropriate uncertainties. We verified that this mirroring method, when applied to non-truncated γ distributions, well reproduced the mean and uncertainty values adopted from our original sampling.

In four of our five identified triple-star systems, only one stellar companion was recovered through our *Gaia* DR3 companion vetting search. This is likely because two of the stellar components have a small enough sky-projected separation such that the stars are blended within the *Gaia* DR3 catalogue. Nevertheless, the configuration of two stellar components still offers useful

geometric insights. Therefore, we calculated γ for these triple-star systems in the same manner that we did for the binary star systems. For V1298 Tau, the triple-star system in our sample that has two resolved stellar components, we calculated γ between the primary and each of the two stellar companions.

2.5. 3D orbit fitting for binary systems

We also carried out 3D orbit fits to derive orbital inclinations for each binary star system using constraints drawn from *Gaia* DR3. Deriving inclinations adds an extra layer of complexity relative to directly examining γ , which is a simple combination of direct observables from *Gaia*. However, orbit forward modeling offers the advantage of explicitly accounting for the range of potential system eccentricities.

To determine binary system inclinations, we first derived posterior distributions for the masses of all stellar companions identified within our search using the *isoclassify* Python package (Huber 2017; Huber et al. 2017; Berger et al. 2020) in “grid” mode. An all-sky dust model drawn from the *mw dust* Python package (Bovy et al. 2016) was applied to account for extinction in all of our *isoclassify* models. For completeness, we included the triple-star system companions within our list of companions for which we derived masses; however, these were excluded from our inclination study, which was explicitly designed to fit binary system orbits.

All inputs to the *isoclassify* code were drawn from *Gaia* DR3. These included stellar parallaxes; G , Bp , and Rp magnitudes; and T_{eff} , $\log g$, and $[\text{Fe}/\text{H}]$ where available, as well as associated uncertainties. The *Gaia* G band, which was available for all sources, was uniformly adopted as the model’s reference absolute magnitude. An uncertainty floor of 5% was adopted for T_{eff} , $\log g$, and $[\text{Fe}/\text{H}]$ – a conservative bound loosely based upon the systematic stellar parameter uncertainty floors described in Tayar et al. (2022). A minimum photometric uncertainty of 1 mag was also set for each band of observations to ensure that the model grid converged on solutions for all systems. The results of this stellar companion mass derivation are provided in Table 1.

Leveraging our newly measured stellar masses, we then used the *lofti_gaia* Python package (Pearce et al. 2020), together with the *Gaia* DR3 catalogue, to uniformly fit the 3D orbits of all binary systems within our sample. In brief, *lofti_gaia* draws astrometric parameters from a selected *Gaia* catalogue to probabilistically determine the allowed orbital properties of binary star systems using the Orbits For The Impatient (OFTI) Bayesian rejection sampling method (Blunt et al. 2017).

Table 1. Candidate stellar companion properties, with masses derived within this work.

Companion name	RA, Dec (°)	Mass (M_{\odot})
Binaries:		
55 Cnc B	(133.167832, 28.315252)	$0.30^{+0.10}_{-0.08}$
CoRoT-2 B	(291.776504, 1.382666)	$0.42^{+0.05}_{-0.07}$
CoRoT-11 B	(280.686736, 5.938083)	$0.96^{+0.36}_{-0.17}$
DS Tuc B	(354.914601, -69.194596)	0.62 ± 0.04
EPIC 246851721 B	(78.918645, 16.277509)	$0.56^{+0.10}_{-0.12}$
HAT-P-1 B	(344.441521, 38.674035)	$1.10^{+0.14}_{-0.12}$
HAT-P-3 B	(206.097634, 48.027322)	$0.22^{+0.06}_{-0.05}$
HAT-P-4 B	(229.999935, 36.205037)	$1.10^{+0.12}_{-0.11}$
HAT-P-7 B	(292.248787, 47.969545)	$0.38^{+0.12}_{-0.11}$
HAT-P-16 B	(9.566866, 42.467720)	0.79 ± 0.05
HAT-P-18 B	(256.346282, 33.011584)	$0.21^{+0.08}_{-0.06}$
HAT-P-20 B	(111.915081, 24.337609)	0.58 ± 0.11
HAT-P-22 B	(155.683035, 50.131058)	0.59 ± 0.11
HAT-P-24 B	(108.825344, 14.261251)	0.44 ± 0.11
HAT-P-30 B	(123.949918, 5.837933)	$0.58^{+0.10}_{-0.11}$
HAT-P-41 B	(297.322581, 4.671410)	0.78 ± 0.12
HAT-P-70 B	(74.547537, 9.968233)	$0.27^{+0.09}_{-0.08}$
HD 189733 B	(300.179016, 22.708365)	0.37 ± 0.01
HD 80606 B	(140.665938, 50.603920)	$0.99^{+0.10}_{-0.08}$
K2-29 B	(62.671159, 24.402645)	$0.74^{+0.05}_{-0.06}$
KELT-9 B	(307.863809, 39.936958)	$0.17^{+0.06}_{-0.04}$
KELT-19 B	(111.505335, 7.605828)	0.43 ± 0.11
KELT-24 B	(161.909223, 71.655152)	$0.61^{+0.12}_{-0.11}$
Kepler-25 B	(286.635515, 39.488638)	$0.77^{+0.05}_{-0.04}$
Kepler-89 B	(297.335668, 41.890478)	$0.72^{+0.05}_{-0.06}$
MASCARA-4 B	(147.577967, -66.114780)	$0.66^{+0.11}_{-0.10}$
Qatar-6 B	(222.210231, 22.151290)	$0.31^{+0.11}_{-0.08}$
TOI-1937 B	(116.370639, -52.382569)	$0.54^{+0.11}_{-0.14}$
TrES-1 B	(286.036339, 36.632911)	$0.16^{+0.06}_{-0.04}$
TrES-4 B	(268.304338, 37.212170)	$0.66^{+0.11}_{-0.10}$
WASP-1 B	(5.167002, 31.991244)	$0.37^{+0.11}_{-0.10}$
WASP-8 B	(359.901133, -35.032571)	$0.54^{+0.10}_{-0.12}$
WASP-14 B	(218.276917, 21.897881)	$0.20^{+0.07}_{-0.05}$
WASP-18 B	(24.350742, -45.684744)	0.15 ± 0.03
WASP-26 B	(4.605675, -15.270848)	0.79 ± 0.05
WASP-33 B	(36.679047, 37.573440)	$0.28^{+0.10}_{-0.08}$
WASP-49 B	(91.089756, -16.966021)	$0.41^{+0.16}_{-0.11}$
WASP-78 B	(63.767405, -22.121908)	0.70 ± 0.04
WASP-85 B	(175.908426, 6.563716)	$0.87^{+0.16}_{-0.11}$
WASP-87 B	(185.327006, -52.842570)	$0.84^{+0.08}_{-0.06}$
WASP-94 B	(313.788298, -34.135730)	$1.14^{+0.10}_{-0.11}$
WASP-100 B	(68.959535, -64.028133)	0.45 ± 0.11
WASP-111 B	(328.769230, -22.612847)	$0.65^{+0.11}_{-0.10}$
WASP-127 B	(160.547657, -3.836883)	$0.96^{+0.09}_{-0.08}$
WASP-167 B	(196.020884, -35.534295)	$1.01^{+0.15}_{-0.09}$
WASP-180 B	(123.393133, -1.983806)	0.77 ± 0.05
WASP-189 B	(225.689198, -3.030630)	$0.52^{+0.11}_{-0.14}$
XO-2 S	(117.030969, 50.216885)	$0.98^{+0.09}_{-0.08}$
Triples:		
K2-290 C	(234.857890, -20.202025)	$0.17^{+0.06}_{-0.04}$
Kepler-13 C	(286.970924, 46.868299)	$1.68^{+0.53}_{-0.43}$
V1298 Tau B	(61.309824, 20.139244)	$0.98^{+0.12}_{-0.11}$
WASP-11 C	(47.367252, 30.677693)	$0.61^{+0.49}_{-0.36}$
WASP-24 C	(227.209554, 2.342041)	$0.36^{+0.06}_{-0.07}$

The user inputs to `lofti_gaia` included the known primary star masses and uncertainties,⁵ as well as our newly derived secondary star masses and uncertainties (Table 1). Where mass uncertainties were asymmetric, we adopted the larger uncertainty for use in `lofti_gaia`. Each model fit was run up to 1000 accepted orbits, and the posterior distribution of orbital parameters was then drawn from the set of accepted solutions. The median inclination and the minimum and maximum 68% credible interval for each system are reported as the central value and uncertainties, respectively, in Table 2.

3. RESULTS

The derived distribution of multi-star system orientations is shown in Figures 3 and 4, and the final set of systems and associated properties is provided in Table 2. Figure 3 shows the distribution of sky-projected spin-orbit angles λ as a function of the sky-projected orbit-orbit angle γ between the primary and secondary star, while Figure 4 replaces γ with the binary inclination i as derived in Section 2.5. Triple-star systems are excluded from Figure 4 because the orbit-fitting method used to extract inclinations is designed for binary star systems. Note that in Figure 3, an edge-on orbit is signified by $\gamma \sim 0^\circ$ or $\gamma \sim 180^\circ$, whereas an edge-on orbit in Figure 4 has $i \sim 90^\circ$. We discuss the implications of these key figures throughout the following sections.

3.1. A population of fully aligned systems

A primary result of this work is the discovery of an overabundance of systems that are consistent with joint orbit-orbit and spin-orbit alignment. We identify seven binary star systems and one triple-star system that robustly fit into this group, shown in the bottom left corner of Figure 3 and the bottom center of Figure 4. All seven systems are part of our “strict” sample and have:

1. a small sky-projected spin-orbit angle consistent with $|\lambda| \leq 10^\circ$ within 1σ ;
2. a sky-projected orbit-orbit angle γ within 10° of either 0° or 180° at the 1σ level, such that $90^\circ - |\gamma - 90^\circ| \leq 10^\circ$ between the planet-hosting star and its *Gaia*-resolved stellar companion;
3. binary inclinations within 10° of an edge-on configuration, such that $|90^\circ - i| \leq 10^\circ$ within 1σ ;

⁵ Primary star masses and uncertainties were set as the default parameter values in the NASA Exoplanet Archive PSCCompPars table on 2023-02-09 (NASA Exoplanet Archive 2023).

Table 2. Source IDs (SIDs) and adopted geometric properties for binary and triple-star systems examined within this work. For the triple-star systems, only the two closest-separation, *Gaia*-resolved sources are listed. Sky-projected orbit-orbit angles γ and inclinations i were each derived within this work. Systems identified as “fully aligned” are denoted with an asterisk. Covariances between RA, Dec, and parallax were not considered when deriving uncertainties for each binary pair separation.

Host star	<i>Gaia</i> DR3 SID, primary	<i>Gaia</i> DR3 SID, cpn	sep (au)	$ \lambda (^{\circ})$	Reference, λ	$\gamma(^{\circ})$	$i(^{\circ})$
Binaries:							
55 Cnc	704967037090946688	704966762213039488	1065 ± 1	10^{+17}_{-20}	Zhao et al. (2023)	33.2 ± 0.2	$68.1^{+10.0}_{-8.1}$
*CoRoT-2	4287820848378092672	4287820852697823872	858 ± 13	$1.0^{+7.7}_{-6.0}$	Czesla et al. (2012)	168.8 ± 4.4	$85.3^{+4.2}_{-3.3}$
CoRoT-11	4285511294172309504	4285511294152417408	1749 ± 384	0.1 ± 2.6	Gandolfi et al. (2012)	100.3 ± 15.4	$51.9^{+15.6}_{-14.1}$
*DS Tuc A	6387058411482257536	6387058411482257280	236 ± 12	$12.1^{+2.6}_{-2.1}$	Benatti et al. (2021)	7.6 ± 0.5	96.1 ± 1.5
EPIC 246851721	3393939030531019520	3393939026238329216	2922 ± 732	$1.47^{+0.86}_{-0.87}$	Yu et al. (2018)	63.9 ± 11.7	$36.6^{+15.1}_{-22.9}$
*HAT-P-1	1928431764627661440	1928431764627661312	1807 ± 33	3.7 ± 2.1	Johnson et al. (2008)	7.4 ± 3.4	$91.6^{+2.8}_{-2.5}$
HAT-P-3	1510191594552968832	1510191594552968960	1346 ± 107	21.2 ± 8.7	Mancini et al. (2018)	72.2 ± 13.1	$107.5^{+9.2}_{-10.8}$
HAT-P-4	1291120362349158016	1291119606434912384	29820 ± 150	4.9 ± 11.9	Winn et al. (2011)	108.4 ± 10.7	$134.8^{+14.7}_{-15.5}$
HAT-P-7	2129256395211984000	2129256395213382272	1362 ± 2137	177.5 ± 9.4	Winn et al. (2009)	5.4 ± 38.6	$79.0^{+24.5}_{-27.7}$
HAT-P-16	381592313648387200	381592519806816896	5136 ± 31	10 ± 16	Moutou et al. (2011)	97.2 ± 1.9	$21.9^{+7.3}_{-12.8}$
HAT-P-18	1334573817793362560	1334573817793501696	415 ± 2178	132 ± 15	Esposito et al. (2014)	127.8 ± 17.7	$60.7^{+18.3}_{-11.4}$
HAT-P-20	869913435026514688	869913430731341440	595 ± 509	8.0 ± 6.9	Esposito et al. (2017)	108.8 ± 6.5	$26.0^{+12.8}_{-12.4}$
*HAT-P-22	846946629987527168	846946625690867328	743 ± 23	2.1 ± 3.0	Mancini et al. (2018)	10.1 ± 0.8	$89.2^{+0.7}_{-0.6}$
HAT-P-24	3167323052618369408	3167323048322924672	2241 ± 692	20 ± 16	Albrecht et al. (2012)	78.2 ± 35.0	$62.7^{+23.4}_{-27.9}$
HAT-P-30	3096441729861716224	3096441729861715968	808 ± 55	73.5 ± 9.0	Johnson et al. (2011)	78.1 ± 1.8	$135.6^{+14.4}_{-13.2}$
HAT-P-41	4290415081653653632	4290415081653653376	1239 ± 50	$22.1^{+6.0}_{-0.8}$	Johnson et al. (2017)	72.7 ± 2.9	$51.9^{+16.0}_{-13.4}$
HAT-P-70	3291455819447952768	3291454921799634304	34993 ± 5091	$107.9^{+2.0}_{-1.7}$	Bello-Arufe et al. (2022)	108.0 ± 11.1	$115.1^{+37.0}_{-30.1}$
*HD 189733	1827242816201846144	1827242816176111360	226 ± 3	0.4 ± 0.2	Cegla et al. (2016)	1.7 ± 0.1	88.6 ± 0.4
HD 80606	1019003226022657920	1019003329101872896	1354 ± 7	42 ± 8	Hébrard et al. (2010)	174.3 ± 0.3	$80.8^{+6.5}_{-5.5}$
K2-29	150054788545735424	150054788545735296	775 ± 69	1.5 ± 8.7	Santerne et al. (2016)	151.0 ± 1.0	$126.7^{+13.6}_{-16.7}$
KELT-9	2064327278651198336	2064327205637457024	2679 ± 342	84.8 ± 0.3	Stephan et al. (2022)	30.0 ± 12.9	$68.9^{+20.4}_{-18.4}$
KELT-19 A	3142847477107193344	3142846618113735552	11948 ± 798	$179.7^{+3.8}_{-3.7}$	Sivervd et al. (2017)	1.8 ± 43.6	$90.6^{+38.8}_{-38.4}$
KELT-24	1076970406751899008	1076970406752355584	194 ± 253	$1.2^{+8.2}_{-7.4}$	Hjorth et al. (2019)	43.0 ± 0.8	$147.5^{+12.6}_{-15.5}$
Kepler-25	2100451630105041152	2100451630105040256	2045 ± 56	0.5 ± 5.7	Albrecht et al. (2013)	158.9 ± 1.7	$68.9^{+12.5}_{-10.8}$
Kepler-89	2076970047474270208	2076969841315840768	3620 ± 258	6^{+11}_{-13}	Hirano et al. (2012),	60.4 ± 8.6	$122.3^{+11.3}_{-15.9}$
MASCARA-4	5245968236116294016	5245968236116983552	732 ± 118	109.66 ± 0.14	Zhang et al. (2022)	105.8 ± 1.1	$42.3^{+20.4}_{-10.2}$
*Qatar-6	1265513389372846848	1265513389372846720	478 ± 102	0.1 ± 2.6	Rice et al. (2023)	0.2 ± 1.6	$90.2^{+1.1}_{-1.2}$
TOI-1937	5489726768531119616	5489726768531118848	1056 ± 1834	4.0 ± 3.5	Yee et al. (2023)	86.6 ± 25.8	$59.2^{+19.5}_{-13.1}$
TrES-1	2098964849867337856	2098964884220974592	2465 ± 904	30 ± 21	Narita et al. (2007)	70.2 ± 61.5	$104.5^{+42.0}_{-28.5}$
*TrES-4	4609062308806929152	4609062381822880384	793 ± 4008	6.3 ± 4.7	Narita et al. (2010)	4.5 ± 14.8	$82.0^{+20.5}_{-19.4}$
WASP-1	2862548428079638912	2862548428079638656	1539 ± 1118	59^{+26}_{-99}	Albrecht et al. (2011b)	61.7 ± 6.3	$22.5^{+4.0}_{-14.7}$
WASP-8	2312679845530628096	2312679845529776128	406 ± 52	$143.0^{+1.5}_{-1.6}$	Bourrier et al. (2017)	4.0 ± 0.5	$94.1^{+2.4}_{-2.9}$
WASP-14	1242084170974175232	1242084166679297920	1894 ± 89	33.1 ± 7.4	Johnson et al. (2009)	88.0 ± 3.4	$157.4^{+13.7}_{-8.1}$
WASP-18	4955371367334610048	4931352153572401152	2959 ± 804	13 ± 7	Albrecht et al. (2012)	115.2 ± 56.3	$74.3^{+35.7}_{-39.3}$
WASP-26	2416782701664155008	2416782705960292608	3890 ± 34	34^{+26}_{-36}	Albrecht et al. (2012)	16.0 ± 8.6	$86.6^{+4.4}_{-4.6}$
WASP-33	328636019723252096	328636264539126912	18254 ± 2608	111.64 ± 0.28	Watanabe et al. (2022)	159.0 ± 10.2	$68.0^{+35.6}_{-39.4}$
WASP-49	2991284369063612928	2991284162905572992	433 ± 543	54^{+79}_{-58}	Wytttenbach et al. (2017)	143.4 ± 6.0	$110.7^{+11.1}_{-12.6}$
WASP-78	5089851638095503616	5089851638095502592	30995 ± 588	6.4 ± 5.9	Brown et al. (2017)	48.9 ± 17.0	$84.0^{+22.7}_{-28.8}$
WASP-85 A	3909745223886018432	3909745223886018560	206 ± 92	0 ± 14	Močnik et al. (2016)	111.8 ± 0.6	$127.5^{+6.6}_{-9.0}$
WASP-87	6077185317188247936	6077185317188247552	2482 ± 76	8 ± 11	Addison et al. (2016)	166.3 ± 2.0	$82.9^{+6.2}_{-5.2}$
WASP-94 A	6780546169634170496	6780546169633474944	3190 ± 31	151^{+16}_{-23}	Neveu-VanMalle et al. (2014)	138.6 ± 3.7	$114.5^{+12.0}_{-18.1}$
WASP-100	4675352109659600000	4675352109658261120	1353 ± 1076	79^{+19}_{-10}	Addison et al. (2018)	65.4 ± 13.3	$142.0^{+18.0}_{-16.4}$
WASP-111	6813902839862151936	6813902839862983296	1469 ± 222	5 ± 16	Anderson et al. (2014)	55.4 ± 4.6	$40.3^{+18.2}_{-13.0}$
WASP-127	3778075171162985600	3778075171162986240	6514 ± 14	$150.6^{+8.7}_{-8.1}$	Cristo et al. (2022)	47.8 ± 2.1	$144.4^{+11.3}_{-19.0}$
WASP-167	6154982877300947840	6154960229936153344	35440 ± 319	165.0 ± 5.0	Temple et al. (2017)	93.1 ± 23.0	$48.2^{+20.9}_{-17.6}$
WASP-180 A	3070964117005132416	3070964117005860736	1265 ± 15	157.0 ± 2.0	Temple et al. (2019)	51.5 ± 2.4	$120.8^{+11.2}_{-12.0}$
WASP-189	6339097679918871168	6339097675623770496	959 ± 15	89.3 ± 1.4	Anderson et al. (2018)	40.4 ± 5.7	$75.2^{+9.6}_{-7.5}$
XO-2 N	934346809278715776	934346740559239296	4677 ± 15	7 ± 11	Damasso et al. (2015)	61.5 ± 4.0	$112.2^{+11.0}_{-10.5}$
Triples:							
K2-290	6253844468883543680	6253844464585162880	2735 ± 272	153 ± 8	Hjorth et al. (2021)	75.2 ± 16.2	-
Kepler-13	2130632159136095104	2130632159130638464	552 ± 2687	58.6 ± 2.0	Masuda (2015)	147.2 ± 7.6	-
*V1298 Tau	51886335968692480	51884824140205824	10515 ± 26	4^{+7}_{-10}	Johnson et al. (2022)	4.2 ± 3.2	-
WASP-11	123376685084303360	123376719445431552	2076 ± 62	7 ± 5	Mancini et al. (2015)	97.9 ± 1.7	-
WASP-24	1153682508388170112	1153682508388170496	7117 ± 178	4.7 ± 4.0	Simpson et al. (2011)	66.6 ± 55.5	-

NOTE—Only one of the two λ measurements made in the K2-290 system is provided here; the second measurement, for the inner planet K2-290 b, is significantly less well-constrained at $\lambda = 173^{+45}_{-53}^{\circ}$ (Hjorth et al. 2021).

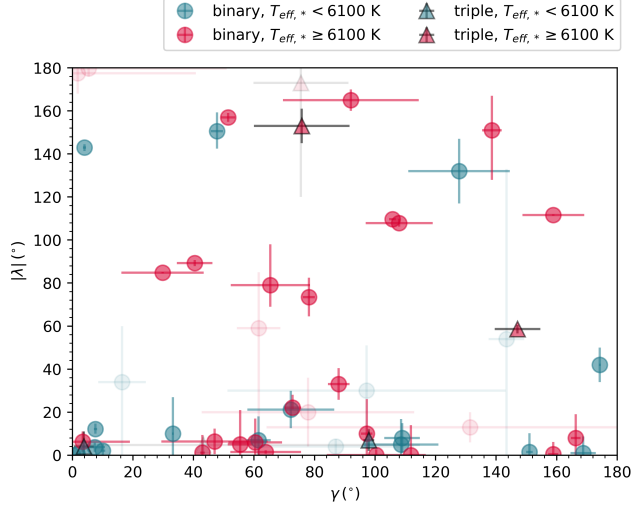


Figure 3. Sky-projected orbit-orbit angle (γ) vs. sky-projected spin-orbit angle (λ) for exoplanets in multi-star systems. For triple-star systems, γ is measured between the primary and the nearest resolved stellar companion. Systems with $\sigma_\gamma > 25^\circ$ and $\sigma_\lambda > 25^\circ$ are shown at low opacity. Systems are colored by the host star’s effective temperature, where the division between “hot” (red) and “cool” (blue) stars is set roughly at the location of the Kraft break.

4. uncertainties $\sigma_\lambda < 25^\circ$, $\sigma_\gamma < 25^\circ$, and, for binary star systems, $\sigma_i < 25^\circ$.

One fully aligned binary system candidate within this population has been previously identified and characterized: Qatar-6 (Rice et al. 2023). In this work, we have identified six additional stellar binary systems that each show evidence of both spin-orbit and orbit-orbit alignment – CoRoT-2, DS Tuc, HAT-P-1, HAT-P-22, HD 189733, and TrES-4. We have also identified one triple-star system, V1298 Tau, that hosts a spin-orbit aligned exoplanet (Johnson et al. 2022; Gaidos et al. 2022) and that exhibits a robust line-of-sight orbit-orbit alignment between the primary and secondary stellar components (the alignment does not extend to the tertiary stellar component). The orbit-orbit alignment in each of these seven systems has been identified for the first time in this work. The V1298 Tau primary star hosts two co-transiting exoplanet companions that are both consistent with spin-orbit alignment.

While this information was not explicitly taken into consideration in our selection criteria, we note that the 3D spin-orbit angles ψ have also been reported for CoRoT-2 b ($\psi = 8.9^{+6.7}_{-5.1}^\circ$), DS Tuc b ($\psi = 4.0^{+4.6}_{-1.6}^\circ$), HAT-P-22 b ($\psi = 6.7^{+29.4}_{-3.8}^\circ$), and HD 189733 b ($\psi = 2.3^{+13.5}_{-1.6}^\circ$) in Albrecht et al. (2021); for V1298 Tau b ($\psi = 8^{+4}_{-7}^\circ$) in Johnson et al. (2022); and for Qatar-6 b

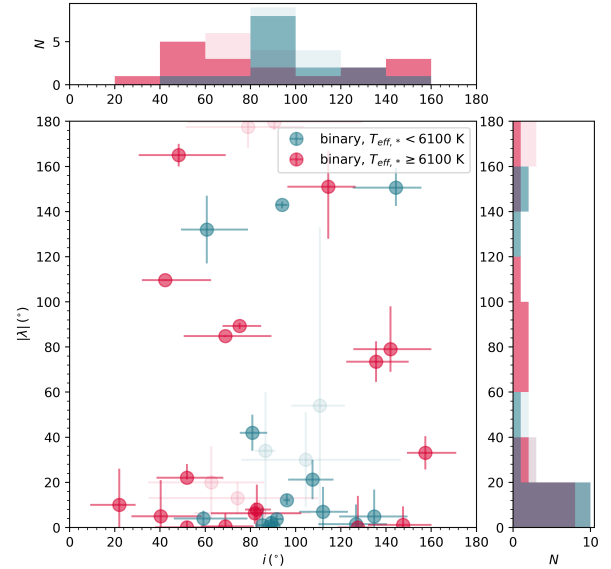


Figure 4. Stellar binary inclination (i) vs. sky-projected spin-orbit angle (λ) for exoplanets in binary star systems. Edge-on binary orbits correspond to $i = 90^\circ$, and all companion planets in the sample have near-edge-on orbits such that they transit the host star. Triple-star systems have been excluded from this figure. Systems with $\sigma_i > 25^\circ$ or $\sigma_\lambda > 25^\circ$ are shown at low opacity. Histograms of the 2D distributions of each parameter are provided in the top and right panels. Both the scatter plot and the histograms are colored by the host star’s effective temperature, as in Figure 3.

($\psi = 21.8^{+8.9}_{-18.4}^\circ$) in Rice et al. (2023). All are consistent with alignment, with $\psi \leq 10^\circ$ within 1σ .

Independent work based on long-term astrometric orbital monitoring recently found one other system, TrES-2, that also demonstrates full spin-orbit and orbit-orbit alignment (Dupuy et al. 2022). The TrES-2 system was removed from our sample at the vetting stage due to the faint magnitude and small projected separation of the companion star ($\rho_0 = 1.1''$ from Dupuy et al. (2022), which corresponds to sky-projected separation $s = 239$ au when combined with the host star’s parallax from *Gaia* DR3), such that it was not resolved in the *Gaia* dataset. This independent discovery offers complementary evidence toward the observed overabundance of aligned systems.

This group of nine systems – including our seven identified fully aligned binary system candidates, TrES-2, and V1298 Tau – comprises a newly discovered population of systems consistent with full spin-orbit and orbit-orbit alignment between the primary and secondary stellar components. The configurations of these systems are

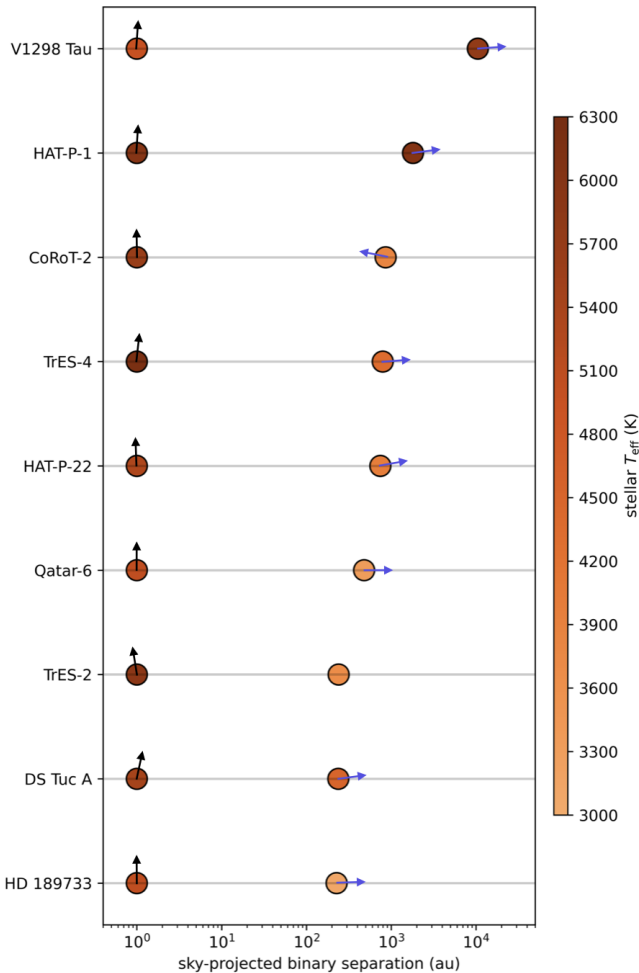


Figure 5. The nine identified “fully aligned” systems, ordered by the sky-projected separation between the exoplanet host star and its aligned companion star. The same color scheme from Figure 1 was used here, with stellar relative velocity vectors shown in blue for all systems with γ measured within this work. All primary, exoplanet-hosting stars are placed at the 1 au mark, with the sky-projected stellar spin axis (as approximated by λ) shown for each host star. Temperatures were drawn from the NASA Exoplanet Archive for exoplanet host stars, and they were drawn either from *Gaia* DR3 or from previously published works (Ngo et al. 2015; Mugrauer 2019) where available for the secondary stars. No previous measurement of T_{eff} was found for TrES-4 B, so the value was estimated from our isochrone fit as $T_{\text{eff}} = 4349^{+521}_{-386}$ K.

shown in Figure 5. Eight of the nine identified systems include an exoplanet host star below the Kraft break ($T_{\text{eff}} \sim 6000 - 6250$ K), a rotational discontinuity above which stars have radiative envelopes (Kraft 1967). As a result, their spin-orbit alignment is consistent with either (1) a primordial coupling between the spin axis and the natal protoplanetary disk (Spalding et al. 2014; Spalding & Batygin 2015) or (2) tidal

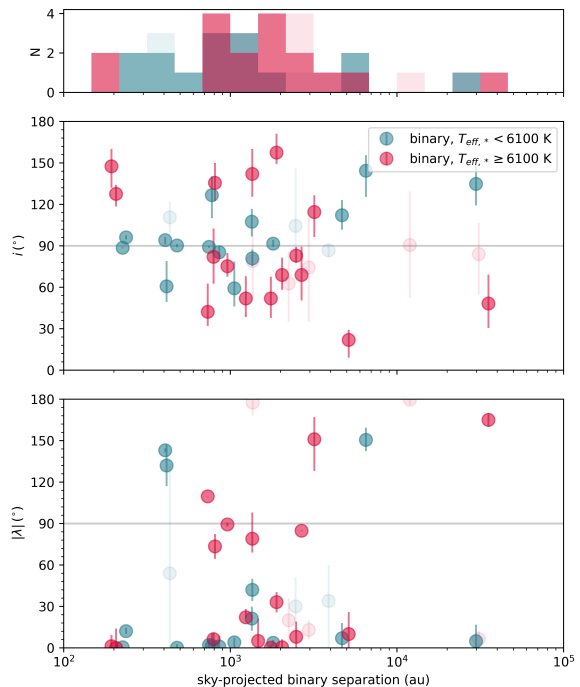


Figure 6. Binary inclination i (top panel) and sky-projected spin-orbit angle $|\lambda|$ (bottom panel) as a function of sky-projected binary separation. The gray lines indicate $i = 90^\circ$ and $|\lambda| = 90^\circ$ for reference. As in Figure 4, systems with $\sigma_i > 25^\circ$ or $\sigma_\lambda > 25^\circ$ are shown at low opacity. Both the scatter plots and the histogram are colored by the host star’s effective temperature, as in Figures 3 and 4.

realignment through dissipation in the convective envelope of the cool host star (Winn et al. 2010; Albrecht et al. 2012; Rice et al. 2022).

The fully aligned sample spans a range of sky-projected stellar separations. Most fully aligned systems have a sky-projected separation $s = 200 - 900$ au between the primary and the secondary star, with two notable exceptions: HAT-P-1, with a sky-projected binary separation $s = 1,806$ au, and V1298 Tau, the aligned triple-star system within our sample, with $s = 10,515$ au between its two aligned components.

3.2. Characterization of the clustering toward alignment

Next, we examined the robustness of the tentative overabundance of fully aligned systems to quantify the likelihood that this population’s alignment arises due to a physical mechanism, rather than by chance. More specifically, we hypothesize that the emergence of a population of fully aligned systems results from viscous

dissipation at the systems’ earlier protoplanetary disk phase (Bate et al. 2000; Lubow & Ogilvie 2000; Foucart & Lai 2014; Zanazzi & Lai 2018). For simplicity, we consider only binary star systems within this section. All systems in the “strict” sample were included within this analysis, including those with large uncertainties $\sigma_i > 25^\circ$ and/or $\sigma_\lambda > 25^\circ$. Our conclusions remain unchanged when these systems are excluded.

We began by building a control sample of binary systems with properties similar to our sample, with the goal of quantifying the robustness of our results to biases that may arise from our orbit-fitting methods. For each system within our “strict” sample, we found the 10 most similar binary star systems in the El-Badry et al. (2021) catalogue, adopting the similarity metric M from Christian et al. (2022):

$$M = \left(\frac{\Delta G_1}{4}\right)^2 + \left(\frac{\Delta G_2}{4}\right)^2 + \left(\frac{\Delta R_{p,1}}{4}\right)^2 + \left(\frac{\Delta R_{p,2}}{4}\right)^2 + \left(\frac{\Delta B_{p,1}}{4}\right)^2 + \left(\frac{\Delta B_{p,2}}{4}\right)^2 + (\Delta \varpi)^2 + (\Delta s)^2. \quad (4)$$

Here, G , B_p , and R_p are the stellar magnitudes provided by *Gaia* DR3, with subscripts for each of the two stars in the system. The projected separation and parallax of the binary system are given as s and ϖ , respectively.

For this control sample, we implemented the same isochrone and orbit fitting process used in Section 2.5 to derive orbital inclinations. For fifteen of the control sample systems, no solution was found with `lofti_gaia` – likely indicating that the systems are either unbound or that one source is a binary – and the systems were discarded. These discarded systems were spread across our comparison sample, with no more than three failed cases from the control sample of any individual star. Therefore, we do not anticipate that removing these samples should significantly bias our results.

The final control sample, which includes 385 systems in total, is shown in teal in Figure 7 alongside the observed distribution of stellar binary inclinations – showing the median values from our orbit fits – and a reference isotropic distribution. In inclination space, $i = 0^\circ$ and $i = 180^\circ$ correspond to perfectly face-on orbits, while $i = 90^\circ$ corresponds to edge-on orbits. Although the control sample distribution lies entirely within the uncertainties derived from our random draws, its profile suggests some modeling bias toward near-edge-on inclinations relative to isotropy. This is an expected outcome of orbit fitting to astrometric observations with short orbital coverage – particularly for orbits that may have significant, nonzero eccentricities – as demonstrated in Section 4 of Ferrer-Chávez et al. (2021).

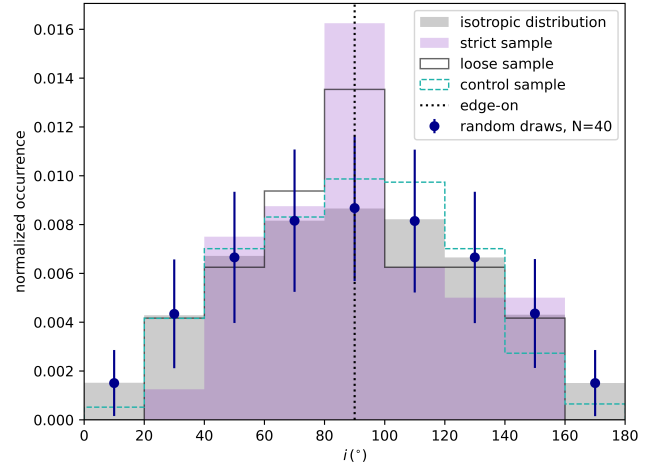


Figure 7. Distribution of observed stellar binary inclinations integrated over all stellar types, compared with inclinations drawn from an isotropic distribution. The “strict” sample is shown in purple, while the “loose” sample and the control sample are shown as black and green unfilled histograms, respectively. The mean and standard deviation of 150,000 random draws from an isotropic distribution, each containing 40 systems (the same number as our “strict” sample), are shown as dark blue error bars.

To quantify the uncertainty associated with the relatively small size of the “strict” sample ($N = 40$), we also derived the mean and standard deviation of 150,000 random draws from an isotropic distribution, where each draw contained 40 systems. The results of these random draws are provided as dark blue error bars in Figure 7. Based on the random draw distribution, the peak toward alignment observed across the full sample is a 2.5σ deviation from the uncertainties associated with the small sample size.

However, our primary observable of interest is not encapsulated solely by the peak toward edge-on orbits: instead, we aim to characterize the overall “peakiness” of the inclination distribution. Viscous dissipation should not only produce a peak toward alignment, but it should also push the full distribution toward a narrower set of inclinations about alignment. This is because, while some systems have already reached orbit-orbit alignment, others, in this framework, should have had their relative orbital inclinations damped (that is, pushed in the direction of orbit-orbit alignment) without reaching full alignment.

Interestingly, in addition to the observed peak toward alignment, we also observe a tentative dearth of near-polar systems, manifesting as an absence of systems in the $i = 0 - 20^\circ$ and $i = 160 - 180^\circ$ bins in Figure 7. To quantify the “peakiness” of the observed distribution, we calculate the fractional difference f between the num-

ber of systems N_{80-100} that fall within the central bin of the distribution ($i = 80 - 100^\circ$) and the number of systems N_{0-20} and $N_{160-180}$ that fall into the two bins that correspond to polar configurations, at $i = 0 - 20^\circ$ and $i = 160 - 180^\circ$, normalized by the total number of systems N_{total} across the full distribution:

$$f = \frac{N_{80-100} - (N_{0-20} + N_{160-180})}{N_{\text{total}}}. \quad (5)$$

This fraction was calculated for each of our samples, as well as for each of the 30,000 random draws used to derive uncertainties in Figure 7. We intentionally exclude the bins between these extremes to avoid systems that are more likely to undergo von Zeipel-Lidov-Kozai (ZLK) (von Zeipel 1910; Lidov 1962; Kozai 1962) oscillations (see Section 3.3 for further discussion on this topic). The results are shown in Figure 8.

The “strict” sample is more centrally peaked than an isotropic distribution at the 3σ level. The control sample also shows, at about the 1σ level, a low-level bias toward a peakier distribution than would be expected from isotropy. While this finding suggests that a portion of the “peakiness” observed within our sample may be attributable to modeling biases, the observed feature is a much stronger outlier than the deviation of the control sample.

3.3. A broader spread of mutual inclinations for hot host stars

Another feature present in our sample is the apparent broader spread of orbit-orbit angles in systems with hot stellar hosts than in systems with cool stellar hosts, as shown in the top histogram of Figure 4. In the case of isotropy, systems with both cool and hot host stars should follow a distribution in binary inclination that is uniform in $\cos i$. By contrast, we observe a strong peak toward alignment in cool star systems ($\mu_{i,\text{cool}} = 100^\circ$; $\sigma_{i,\text{cool}} = 21^\circ$), with no clear peak and broader scatter for hot star systems ($\mu_{i,\text{hot}} = 86^\circ$; $\sigma_{i,\text{hot}} = 37^\circ$). This observation persists when stars with $\sigma_i > 25^\circ$ and $\sigma_\lambda > 25^\circ$ are excluded from the sample; in this case, $\mu_{i,\text{cool}} = 100^\circ$; $\sigma_{i,\text{cool}} = 22^\circ$; $\mu_{i,\text{hot}} = 89^\circ$; and $\sigma_{i,\text{hot}} = 41^\circ$.

The mutual inclination distribution for hot star systems does not appear random, but instead shows two suggestive peaks *away* from isotropy, around $i = 40 - 60^\circ$ and $i = 140 - 160^\circ$. This double-peaked structure is reminiscent of the final mutual inclination distribution anticipated from the ZLK mechanism – as seen in, for example, the bottom left panel of Figure 3 in Naoz et al. (2012). Therefore, we interpret this difference as evidence that, while cool star systems within our sample preferentially display orbit-orbit alignment, the hot

star systems may have preferentially experienced ZLK oscillations.

3.4. No clear correlation between spin-orbit and orbit-orbit misalignment

We find no convincing correlation between spin-orbit and orbit-orbit alignment from our observed population. In particular, with a larger sample and updated parameters from *Gaia* DR3, we do not recover the tentative correlation between spin-orbit and orbit-orbit misalignment suggested by Behrard et al. (2022). Among the current sample of systems within both spin-orbit measurements and robust stellar companions, we find that systems that are spin-orbit misaligned span a wide range of orbit-orbit configurations, and vice versa.

3.5. Significance of the observed trends in the viscous dissipation framework

Throughout all preceding sections, we considered the distribution of mutual orbital inclinations for all stellar companion separations. This choice was deliberate, to remain agnostic to the underlying mechanism producing the observed features in the distribution. Given the observed evidence in favor of (1) several fully aligned systems (Section 3.1), (2) a relatively peaked distribution of binary inclinations (Section 3.2), and (3) a wider spread in the inclination distribution for hot stars (Section 3.3), we hypothesize that the inclination distribution for cool systems in our sample is shaped by viscous dissipation in nodally recessing protoplanetary disks that are warped by a nearby stellar perturber (Bate et al. 2000; Lubow & Ogilvie 2000; Foucart & Lai 2014; Zanazzi & Lai 2018). We again consider only binary systems within this section for consistency with Section 3.2, and we report results for the “strict” sample.

In the viscous dissipation framework, the set of close-to-moderate-separation binaries would experience some inclination damping, while extremely wide-separation binaries would remain relatively unaffected and would instead serve primarily to add noise to our sample. To consider this scenario, we exclude extremely wide-separation binaries in this section, conservatively setting the outer limit for the influence of viscous dissipation to $s = 2,000$ au.

We applied the Kuiper statistic version of the Kolmogorov-Smirnov test to examine the significance of our observed trends for binaries with $s < 2,000$ au. Specifically, we conducted one-sample Kuiper tests comparing the observed and/or control sample of binary inclinations to an isotropic distribution (uniform in $\cos i$), as well as two-sample Kuiper tests to compare subsets of the observed and/or control samples with each other.

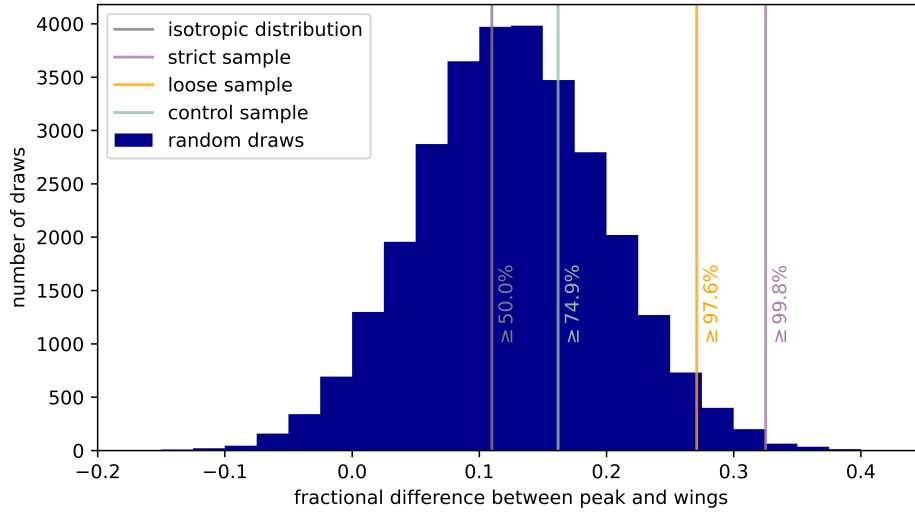


Figure 8. Distribution of the fractional difference f between systems located within the $i = 80 - 100^\circ$ bin and those located in the $i = 0 - 20^\circ$ or $i = 160 - 180^\circ$ bins in Figure 7. The dark blue histogram is comprised of the same 30,000 random draws used to produce error bars in Figure 7. Based on the distribution of f , the “strict” sample is more centrally peaked toward edge-on than an isotropic distribution at the $\sim 3\sigma$ level.

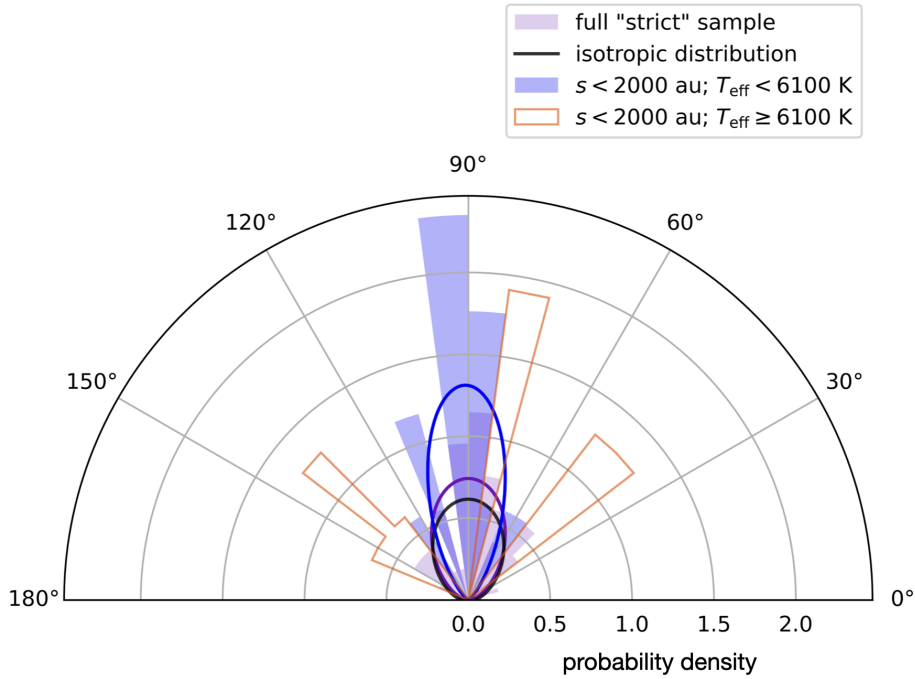


Figure 9. Normalized distribution of inclinations for the “strict” sample (purple filled histogram) with no s or T_{eff} cuts, as well as the more restricted hot star (orange outline) and cool star (blue filled histogram) samples for comparison. Overplotted in the same colors are the maximum-likelihood von Mises probability density functions fitted to the full “strict” sample ($\mu = 90.0^\circ$; $\kappa = 3.8$) and to the cool star subset sample ($\mu = 90.8^\circ$; $\kappa = 11.1$), each of which demonstrates a single peak. The von Mises probability density function for a simulated isotropic distribution, with 30,000 draws as in Figure 7, is shown in black for reference, with $\mu = 90.0^\circ$ and $\kappa = 2.7$.

In each case, the null hypothesis – that both samples are drawn from the same underlying distribution – can be rejected if the p -value associated with the Kuiper test is $p < 0.05$. Each inclination distribution was characterized as $|\cos i|$ such that values fall within the range $0 \leq |\cos i| \leq 1$ and alignment corresponds to $|\cos i| = 0$, while polar orbits correspond to $|\cos i| = 1$.

First, the observed sample and the control sample were compared to show whether they demonstrably arise from separate distributions. We drew from the control sample in 30,000 iterations to match the number of systems in each observed sample, then found the median of the p -values from all iterations. The two-sample Kuiper test accepts the null hypothesis that both samples are drawn from the same underlying distribution, with $p = 0.50$. This suggests that the underlying distributions do not strongly deviate from each other. The one-sample Kuiper test also accepts the null hypotheses that the full observed sample ($p = 0.65$) and the control sample ($p = 0.28$) are each consistent with isotropy.

A series of Kuiper tests further affirms the observations outlined in Section 3.3. A two-sample Kuiper test strongly rejects the null hypothesis that the cool and hot star systems within our sample stem from the same inclination distribution, with $p = 0.004$. When the same test is run between the hot and cool comparison stars in the control sample – which includes binaries at a wide range of separations – the null hypothesis is accepted with $p = 0.39$. Furthermore, the one-sample Kuiper test rejects the null hypothesis that cool stars are drawn from an isotropic distribution ($p = 0.04$), while it marginally accepts the null hypothesis that hot stars are drawn from an isotropic distribution ($p = 0.09$). Therefore, although the full sample is consistent with isotropy, the two subsamples drawn from it appear to be distinct and marginally inconsistent with isotropy. Ultimately, we conclude that the cool and hot star systems in our sample demonstrate separate inclination distributions, with cool star systems showing a “peakier” distribution toward alignment, while hot star systems demonstrate broader scatter in their orbit-orbit orientations.

The distributions of cool and hot star samples examined within this section are shown in Figure 9, alongside the full “strict” sample for reference. While the hot star population, in orange, visibly deviates from a single overdensity, both the full sample and the cool star sample show peaks toward $i = 90^\circ$. We fit the von Mises distribution, a wrapped Gaussian on a circle, to each of these two peaked distributions, following the probability density function

$$f(x|\mu, \kappa) = \frac{\exp(\kappa \cos(x - \mu))}{2\pi I_0(\kappa)} \quad (6)$$

where μ signifies the directionality of the distribution’s peak; κ is a measure of uniformity in which large values indicate higher concentration; and $I_0(\kappa)$ is the modified Bessel function of order zero. We find that the full “strict” sample is best fit by a von Mises probability density function with $\mu = 90.0^\circ$ and $\kappa = 3.9$. When only the cool stars with nearby companions are considered, the location of the peak stays roughly static at $\mu = 90.8^\circ$, while the concentration toward the peak is much more pronounced ($\kappa = 11.1$). For comparison, a von Mises fit to an isotropic distribution of inclinations is also shown, with a resulting peak at $\mu = 90.0^\circ$ with $\kappa = 2.7$.

Finally, a Kuiper test confirms that, as suggested in Section 3.5, no clear correlation is found between spin-orbit misalignment and orbit-orbit misalignment. A two-sample Kuiper test comparing the inclinations of systems with $\lambda > 25^\circ$ to systems with $\lambda \leq 25^\circ$ is accepted with $p = 0.58$.

4. DISCUSSION

The results presented within this work suggest that viscous dissipation may be relatively efficient for some subset of planetary systems. While only eight of the 40 systems within our “strict” sample exhibit evidence of full alignment, the peaked distribution of inclinations suggests that many systems are pushed in the direction of alignment at some point during the system lifetimes. Fully aligned systems can be reproduced through strong viscous dissipation during the protoplanetary disk stage, together with star-disk coupling and an absence of resonant crossings or strong post-disk planet-planet interactions.

Within the viscous dissipation framework, the widest-separation fully aligned systems identified in this work may represent chance orbit-orbit alignments in the line-of-sight direction. The HAT-P-1 and V1298 Tau systems have sky-projected separation $s = 1,806$ au and $s = 10,515$ au, respectively, between their two aligned components. Because the viscous damping rate scales as $\gamma_b \propto a_b^{-6}$ for true binary separations a_b (Zanazzi & Lai 2018), HAT-P-1 and V1298 Tau each have relatively long orbit-orbit alignment timescales by comparison with the other fully aligned systems in our sample. Given the prevalence of spin-orbit aligned systems within our sample, a joint spin-orbit and line-of-sight orbit-orbit alignment for one or both systems could plausibly arise by chance from the independent evolution of the two stars in each of the systems.

The broader range of inclinations observed in hot star systems as compared with cool star systems may also offer dynamical insights into the underlying properties

of protoplanetary disk systems. Within the viscous dissipation framework, the observed difference in the inclination distribution could arise due to systematic differences in disk extent, aspect ratio, and viscosity. For example, protoplanetary disks around low-mass stars may have a lower temperature and therefore lower aspect ratio, enabling them to dissipate energy more efficiently than disks around high-mass stars. Differences in the protoplanetary disk dispersal timescales for cool and hot star systems may produce systematic differences in their final geometries, as well: previous work has shown that high-mass stars have systematically shorter protoplanetary disk lifetimes than lower-mass stars (Ribas et al. 2015), likely due to differences in the dispersal rate of disk material through viscous accretion, magnetohydrodynamic winds, and photoevaporation as a function of stellar type (Komaki et al. 2021, 2023). Hot star systems would, therefore, have less time available to realign prior to protoplanetary disk dispersal.

We emphasize that, because of the relatively deep transits that are necessary to resolve the Rossiter-McLaughlin effect or Doppler tomography signals, our sample is dominated by systems that host short-period giant planets. As a result, our sample is not representative of the full breadth of system types. Instead, the presented results are biased toward systems that likely had relatively high-mass and/or high-metallicity natal protoplanetary disks. Further joint spin-orbit and orbit-orbit analyses for systems with smaller, lower-mass planets are necessary to characterize the generality of the trends examined within this work.

5. CONCLUSIONS

In this work, we examined the joint spin-orbit and orbit-orbit distribution for exoplanets residing in binary and triple-star systems. We considered the full sample of systems with both (1) an exoplanet spin-orbit measurement within the TEPcat catalogue and (2) one or more stellar companions resolved by *Gaia* DR3. Our conclusions are as follows:

- We identify a population of nine exoplanet host systems that each exhibit evidence of joint spin-orbit and orbit-orbit alignment. The joint alignment of seven of these systems was demonstrated for the first time: six binary star systems (CoRoT-2, DS Tuc, HAT-P-1, HAT-P-22, HD 189733, and TrES-4) were found to exhibit evidence of full system alignment, and one triple-star system (V1298 Tau) exhibits evidence of full alignment between the host star’s transiting exoplanet companion and one of the two companion stars.

- The sample of stellar binary inclinations for exoplanet-hosting systems with spin-orbit constraints is more strongly peaked toward alignment than an isotropic distribution – a trend that appears to be driven largely by cool host star ($T_{\text{eff}} < 6100$ K) systems within the sample. We find a joint overabundance of systems demonstrating line-of-sight orbit-orbit alignment and underabundance of face-on systems that correspond to near-polar binary orbital configurations. This observed trend may be a signature of viscous dissipation induced by nodal recession during the protoplanetary disk phase.
- For the set of systems with $s < 2,000$ au, we demonstrate a broader spread in orbit-orbit orientations observed in hot star systems than in cool star systems. Eight of the nine observed fully aligned systems also include a cool host star below the Kraft break. In the viscous dissipation framework, these observations provide evidence that protoplanetary disks around cool stars may be longer-lived and/or more efficient at dissipating energy than those around hot stars.
- No clear correlation is found between spin-orbit misalignment and orbit-orbit misalignment. This result indicates that, while mechanisms related to spin-orbit excitation may, in some cases, be enhanced by orbit-orbit misalignments, orbit-orbit misalignment does not necessarily accompany spin-orbit misalignment (and vice versa).

Our results highlight an observed regime within which moderately wide-separation stellar companions push their neighbors’ protoplanetary disks, and therefore the planetary systems that emerge from those disks, toward an aligned state, approaching a more general three-body equilibrium (Hut 1981) and enhancing order in exoplanet systems. Further observations of similar, well-constrained systems offer the potential to provide precise dynamical limits on protoplanetary disk properties, offering a new lens through which disk properties – including masses, viscosities, and lifetimes – may be constrained.

6. ACKNOWLEDGEMENTS

We thank J. J. Zanazzi, Songhu Wang, Sam Christian, Fei Dai, Aida Behmard, Smadar Naoz, and Matthew Bate for helpful discussions over the course of this work. M.R. acknowledges support from Heising-Simons Foundation Grant #2023-4478, as well as the 51 Pegasi b Fellowship Program. This research has made

use of the NASA Exoplanet Archive, which is operated by the California Institute of Technology, under contract with the National Aeronautics and Space Administration under the Exoplanet Exploration Program. This work has made use of data from the European Space Agency (ESA) mission *Gaia* (<https://www.cosmos.esa.int/gaia>), processed by the *Gaia* Data Processing and Analysis Consortium (DPAC, <https://www.cosmos.esa.int/web/gaia/dpac/consortium>). Funding for the DPAC has been provided by national institu-

tions, in particular the institutions participating in the *Gaia* Multilateral Agreement.

Software: `numpy` (Oliphant 2006; Walt et al. 2011; Harris et al. 2020), `matplotlib` (Hunter 2007), `pandas` (McKinney 2010), `lofti_gaia` (Pearce et al. 2020), `isoclassify` (Huber 2017; Huber et al. 2017; Berger et al. 2020), `mwdust` (Bovy et al. 2016), `scipy` (Virtanen et al. 2020), `astropy` (Astropy Collaboration et al. 2013, 2018, 2022)

Facility: NASA Exoplanet Archive, Extrasolar Planet Encyclopaedia, TEPcat

APPENDIX

A. JOINT ALIGNMENT CANDIDATES

While building the final samples for this study, we identified several candidates for joint spin-orbit and orbit-orbit alignment that nearly satisfy the four robustness tests described in Section 3.1, but that were removed from the final sample in this work due to less well-constrained orbits that manifest as relatively large uncertainties. We classify these systems as “joint alignment candidates” and discuss their properties here.

Several joint alignment candidates were identified from the sample of binary star systems examined within this work. WASP-26 satisfies Conditions 1, 2, and 3 but has too weak a spin-orbit constraint ($\lambda = -34_{-26}^{+36} \circ$) to conclusively determine whether the host star’s companion exoplanet is spin-orbit aligned. WASP-87 meets all conditions except Condition 2, such that the system may be near, but not exactly, edge-on in γ . Four further systems (HAT-P-24, TrES-1, WASP-18, and WASP-78) meet Conditions 1 and 3 but have relatively large uncertainties such that they are not unambiguously edge-on in either γ or i . Further astrometric monitoring or radial velocity measurements between the two binary components would help to conclusively determine whether these four systems are edge-on.

One additional triple-star system, WASP-24, hosts an aligned planetary companion and may be consistent with orbit-orbit alignment. Only two of the three stars in the WASP-24 system are resolved in *Gaia* DR3: the secondary component was identified as an eclipsing binary in Street et al. (2010). However, the large uncertainty in γ between the two resolved stars within the WASP-24 system ($\sigma_\gamma = 55.5 \circ$) renders the measurement of γ relatively uninformative, such that the system’s true alignment remains ambiguous.

All joint alignment candidates discussed in this section are present in both the “strict” and “loose” samples. No additional joint alignment candidates were found in the “loose” sample that are not present in the “strict” sample.

B. TRIPLE-STAR SYSTEMS

Five triple-star systems emerged from our sample vetting: K2-290, Kepler-13, V1298 Tau, WASP-11, and WASP-24. In this section, we discuss the geometric properties of these systems in greater detail.

Of the five systems identified as triple-star systems within this work, four had both stellar companions identified in previous publications. WASP-11 and WASP-24 were shown to be bound triple-star systems by Mugrauer (2019), while Kepler-13 was identified as a triple-star system by Santerne et al. (2012) and K2-290 was identified as a triple-star system in the discovery paper for its two companion planets (Hjorth et al. 2019). Each of these four systems has only two stellar components resolved by *Gaia* DR3, likely due to the relatively close separation of the third component in each case. Kepler-13 BC is a spectroscopic binary (Johnson et al. 2014), while WASP-24 BC is an eclipsing binary (Street et al. 2010; Mugrauer 2019). K2-290 B is located at a separation of only $0.4''$ from the primary star (Hjorth et al. 2019) and HAT-P-10 B is only $0.36''$ from the primary star (Ngo et al. 2015), such that both stars are likely unresolved by *Gaia* DR3.

V1298 Tau, by contrast, has not been previously confirmed as a triple-star system. Of the five identified systems, V1298 Tau is also the only one that has all three stellar components resolved by *Gaia* DR3. David et al. (2019) conducted several robustness tests searching for close-in companions but identified none. Our results are consistent with the absence of nearby ($s < 10,000$ au) stellar companions in the V1298 Tau system.

We observe that the more nearby stellar companion to V1298 Tau, at $s = 10,515$ au, is consistent with alignment ($\gamma = 4.2 \pm 3.2^\circ$), while the further companion at $s = 14,632$ au is likely misaligned at $\gamma = 125.5 \pm 4.4^\circ$. The close alignment of such a distant companion in this system is surprising and challenging to reproduce through dissipative channels over the expected lifetime of a protoplanetary disk. Therefore, it is possible that the line-of-sight orbit-orbit alignment observed in the V1298 Tau system may reflect a chance alignment.

All resolved companions in the identified triple-star systems were identified at relatively wide sky-projected separations $s > 2,000$ au from the primary, with the exception of Kepler-13, which has a secondary companion at $s = 552$ au. Kepler-13 b is spin-orbit misaligned ($|\lambda| = 58.6 \pm 2.0^\circ$) and the secondary star has $\gamma = 147.2 \pm 7.6^\circ$ relative to the primary, indicating that the secondary star's orbital plane is likely not edge-on.

REFERENCES

- Adams, F. C., Ruden, S. P., & Shu, F. H. 1989, *ApJ*, 347, 959
- Addison, B., Tinney, C., Wright, D., & Bayliss, D. 2016, *The Astrophysical Journal*, 823, 29
- Addison, B., Wang, S., Johnson, M., et al. 2018, *The Astronomical Journal*, 156, 197
- Albrecht, S., Winn, J. N., Carter, J. A., Snellen, I. A. G., & de Mooij, E. J. W. 2011a, *ApJ*, 726, 68
- Albrecht, S., Winn, J. N., Marcy, G. W., et al. 2013, *The Astrophysical Journal*, 771, 11
- Albrecht, S., Winn, J. N., Johnson, J. A., et al. 2011b, *ApJ*, 738, 50
- Albrecht, S., Winn, J. N., Johnson, J. A., et al. 2012, *ApJ*, 757, 18
- Albrecht, S. H., Dawson, R. I., & Winn, J. N. 2022, *PASP*, 134, 082001
- Albrecht, S. H., Marcussen, M. L., Winn, J. N., Dawson, R. I., & Knudstrup, E. 2021, *ApJL*, 916, L1
- Anderson, D., Brown, D., Cameron, A. C., et al. 2014, *arXiv preprint arXiv:1410.3449*
- Anderson, D. R., Collier Cameron, A., Hellier, C., et al. 2011a, *ApJL*, 726, L19
- . 2011b, *A&A*, 531, A60
- Anderson, D. R., Temple, L. Y., Nielsen, L. D., et al. 2018, *arXiv e-prints*, arXiv:1809.04897
- Astropy Collaboration, Robitaille, T. P., Tollerud, E. J., et al. 2013, *A&A*, 558, A33
- Astropy Collaboration, Price-Whelan, A. M., Sipőcz, B. M., et al. 2018, *AJ*, 156, 123
- Astropy Collaboration, Price-Whelan, A. M., Lim, P. L., et al. 2022, *ApJ*, 935, 167
- Bate, M. R. 2000, *MNRAS*, 314, 33
- Bate, M. R., Bonnell, I. A., Clarke, C. J., et al. 2000, *MNRAS*, 317, 773
- Bate, M. R., Lodato, G., & Pringle, J. E. 2010, *MNRAS*, 401, 1505
- Batygin, K. 2012, *Nature*, 491, 418
- Behrard, A., Dai, F., & Howard, A. W. 2022, *AJ*, 163, 160
- Bello-Arufe, A., Cabot, S. H., Mendonça, J. M., Buchhave, L. A., & Rathcke, A. D. 2022, *The Astronomical Journal*, 163, 96
- Belokurov, V., Penoyre, Z., Oh, S., et al. 2020, *MNRAS*, 496, 1922
- Benatti, S., Damasso, M., Borsa, F., et al. 2021, *Astronomy & Astrophysics*, 650, A66
- Berger, T. A., Huber, D., Van Saders, J. L., et al. 2020, *AJ*, 159, 280
- Blunt, S., Nielsen, E. L., De Rosa, R. J., et al. 2017, *AJ*, 153, 229
- Bonnell, I. A., & Bate, M. R. 1994, *MNRAS*, 271, 999. <https://doi.org/10.1093/mnras/271.4.999>
- Bourrier, V., Cegla, H., Lovis, C., & Wyttenbach, A. 2017, *A&A*, 599, A33
- Bovy, J., Rix, H.-W., Green, G. M., Schlafly, E. F., & Finkbeiner, D. P. 2016, *ApJ*, 818, 130
- Brown, D., Triaud, A., Doyle, A., et al. 2017, *Monthly Notices of the Royal Astronomical Society*, 464, 810
- Cegla, H., Lovis, C., Bourrier, V., et al. 2016, *Astronomy & Astrophysics*, 588, A127
- Christian, S., Vanderburg, A., Becker, J., et al. 2022, *AJ*, 163, 207
- Collier Cameron, A., Bruce, V. A., Miller, G. R. M., Triaud, A. H. M. J., & Queloz, D. 2010, *MNRAS*, 403, 151
- Cristo, E., Santos, N. C., Demangeon, O., et al. 2022, *A&A*, 660, A52
- Czesla, S., Schröter, S., Wolter, U., et al. 2012, *Astronomy & Astrophysics*, 539, A150
- Dai, F., Winn, J. N., Yu, L., & Albrecht, S. 2017, *AJ*, 153, 40
- Damasso, M., Biazzo, K., Bonomo, A. S., et al. 2015, *A&A*, 575, A111
- David, T. J., Cody, A. M., Hedges, C. L., et al. 2019, *AJ*, 158, 79
- Dupuy, T. J., Kraus, A. L., Kratter, K. M., et al. 2022, *MNRAS*, 512, 648

- El-Badry, K., Rix, H.-W., & Heintz, T. M. 2021, *MNRAS*, 506, 2269
- Esposito, M., Covino, E., Mancini, L., et al. 2014, *Astronomy & Astrophysics*, 564, L13
- Esposito, M., Covino, E., Desidera, S., et al. 2017, *Astronomy & Astrophysics*, 601, A53
- Ferrer-Chávez, R., Wang, J. J., & Blunt, S. 2021, *AJ*, 161, 241
- Fontanive, C., & Bardalez Gagliuffi, D. 2021, *Frontiers in Astronomy and Space Sciences*, 16
- Foucart, F., & Lai, D. 2014, *MNRAS*, 445, 1731
- Gaia Collaboration, Prusti, T., de Bruijne, J. H. J., et al. 2016, *A&A*, 595, A1
- Gaia Collaboration, Vallenari, A., Brown, A. G. A., et al. 2022, arXiv e-prints, arXiv:2208.00211
- Gaidos, E., Hirano, T., Beichman, C., et al. 2022, *MNRAS*, 509, 2969
- Gandolfi, D., Collier Cameron, A., Endl, M., et al. 2012, *A&A*, 543, L5
- Harris, C. R., Millman, K. J., van der Walt, S. J., et al. 2020, *Nature*, 585, 357
- Hébrard, G., Désert, J.-M., Díaz, R., et al. 2010, *Astronomy & Astrophysics*, 516, A95
- Hirano, T., Narita, N., Sato, B., et al. 2012, *The Astrophysical Journal Letters*, 759, L36
- Hjorth, M., Albrecht, S., Hirano, T., et al. 2021, *Proceedings of the National Academy of Sciences*, 118, e2017418118
- Hjorth, M., Justesen, A. B., Hirano, T., et al. 2019, *MNRAS*, 484, 3522
- Hjorth, M., Albrecht, S., Talens, G., et al. 2019, *Astronomy & Astrophysics*, 631, A76
- Huber, D. 2017, Zenodo, doi, 10
- Huber, D., Zinn, J., Bojsen-Hansen, M., et al. 2017, *ApJ*, 844, 102
- Hunter, J. D. 2007, *Computing in science & engineering*, 9, 90
- Hut, P. 1981, *A&A*, 99, 126
- Johnson, J. A., Winn, J. N., Albrecht, S., et al. 2009, *Publications of the Astronomical Society of the Pacific*, 121, 1104
- Johnson, J. A., Winn, J. N., Narita, N., et al. 2008, *The Astrophysical Journal*, 686, 649
- Johnson, J. A., Winn, J., Bakos, G., et al. 2011, *The Astrophysical Journal*, 735, 24
- Johnson, M. C., Cochran, W. D., Addison, B. C., Tinney, C. G., & Wright, D. J. 2017, *The Astronomical Journal*, 154, 137
- Johnson, M. C., Cochran, W. D., Albrecht, S., et al. 2014, *ApJ*, 790, 30
- Johnson, M. C., David, T. J., Petigura, E. A., et al. 2022, *AJ*, 163, 247
- Kamiaka, S., Benomar, O., Suto, Y., et al. 2019, *AJ*, 157, 137
- Komaki, A., Fukuhara, S., Suzuki, T. K., & Yoshida, N. 2023, arXiv preprint arXiv:2304.13316
- Komaki, A., Nakatani, R., & Yoshida, N. 2021, *ApJ*, 910, 51
- Kozai, Y. 1962, *AJ*, 67, 591
- Kraft, R. P. 1967, *ApJ*, 150, 551
- Krumholz, M. R., Klein, R. I., & McKee, C. F. 2007, *ApJ*, 656, 959
- Lai, D. 2014, *MNRAS*, 440, 3532
- Lester, K. V., Howell, S. B., Matson, R. A., et al. 2023, *AJ*, 166, 166
- Lidov, M. L. 1962, *Planetary and Space Science*, 9, 719
- Lubow, S., & Ogilvie, G. 2000, *ApJ*, 538, 326
- Mancini, L., Esposito, M., Covino, E., et al. 2015, *A&A*, 579, A136
- . 2018, *Astronomy & Astrophysics*, 613, A41
- Masuda, K. 2015, *ApJ*, 805, 28
- Matson, R. A., Howell, S. B., Horch, E. P., & Everett, M. E. 2018, *AJ*, 156, 31
- McKinney, W. 2010, in *Proceedings of the 9th Python in Science Conference*, Vol. 445, Austin, TX, 51–56
- McLaughlin, D. B. 1924, *ApJ*, 60, 22
- Močnik, T., Clark, B., Anderson, D., Hellier, C., & Brown, D. 2016, *The Astronomical Journal*, 151, 150
- Moutou, C., Díaz, R. F., Udry, S., et al. 2011, *Astronomy & Astrophysics*, 533, A113
- Mugrauer, M. 2019, *MNRAS*, 490, 5088
- Naoz, S. 2016, *ARA&A*, 54, 441
- Naoz, S., Farr, W. M., & Rasio, F. A. 2012, *ApJL*, 754, L36
- Narita, N., Sato, B., Hirano, T., et al. 2010, *Publications of the Astronomical Society of Japan*, 62, 653
- Narita, N., Enya, K., Sato, B., et al. 2007, *Publications of the Astronomical Society of Japan*, 59, 763
- NASA Exoplanet Archive. 2023, *Planetary Systems Composite Parameters*, vVersion: 2023-02-09, NExScI-Caltech/IPAC, doi:10.26133/NEA13. <https://catcopy.ipac.caltech.edu/doi/doi.php?id=10.26133/NEA13>
- Neveu-VanMalle, M., Queloz, D., Anderson, D., et al. 2014, *Astronomy & Astrophysics*, 572, A49
- Ngo, H., Knutson, H. A., Hinkley, S., et al. 2015, *ApJ*, 800, 138
- Oliphant, T. E. 2006, *A guide to NumPy*, Vol. 1 (Trelgol Publishing USA)
- Pearce, L. A., Kraus, A. L., Dupuy, T. J., et al. 2020, *AJ*, 894, 115

- Queloz, D., Eggenberger, A., Mayor, M., et al. 2000, *A&A*, 359, L13
- Ribas, Á., Bouy, H., & Merín, B. 2015, *Astronomy & Astrophysics*, 576, A52
- Rice, M., Wang, S., Gerbig, K., et al. 2023, *AJ*, 165, 65
- Rice, M., Wang, S., & Laughlin, G. 2022, *ApJL*, 926, L17
- Rice, M., Wang, S., Howard, A. W., et al. 2021, *AJ*, 162, 182
- Rossiter, R. A. 1924, *ApJ*, 60, 15
- Sanchis-Ojeda, R., & Winn, J. N. 2011, *ApJ*, 743, 61
- Santerne, A., Moutou, C., Barros, S. C. C., et al. 2012, *A&A*, 544, L12
- Santerne, A., Hébrard, G., Lillo-Box, J., et al. 2016, *The Astrophysical Journal*, 824, 55
- Simpson, E. K., Pollacco, D., Cameron, A. C., et al. 2011, *MNRAS*, 414, 3023
- Sivervd, R. J., Collins, K. A., Zhou, G., et al. 2017, *The Astronomical Journal*, 155, 35
- Southworth, J. 2011, *MNRAS*, 417, 2166
- Spalding, C., & Batygin, K. 2015, *ApJ*, 811, 82
- Spalding, C., Batygin, K., & Adams, F. C. 2014, *ApJL*, 797, L29
- Stephan, A. P., Wang, J., Cauley, P. W., et al. 2022, *The Astrophysical Journal*, 931, 111
- Street, R. A., Simpson, E., Barros, S. C. C., et al. 2010, *ApJ*, 720, 337
- Tayar, J., Claytor, Z. R., Huber, D., & van Saders, J. 2022, *ApJ*, 927, 31
- Temple, L. Y., Hellier, C., Albrow, M. D., et al. 2017, *MNRAS*, 471, 2743
- Temple, L. Y., Hellier, C., Anderson, D. R., et al. 2019, *MNRAS*, 490, 2467
- Tobin, J. J., Looney, L. W., Li, Z.-Y., et al. 2016, *ApJ*, 818, 73
- Tokovinin, A. 2020, *MNRAS*, 496, 987
- . 2022, *ApJ*, 926, 1
- Tokovinin, A., & Kiyaveva, O. 2015, *MNRAS*, 456, 2070
- Triaud, A. H. M. J., Collier Cameron, A., Queloz, D., et al. 2010, *A&A*, 524, A25
- Vick, M., Su, Y., & Lai, D. 2023, *ApJL*, 943, L13
- Virtanen, P., Gommers, R., Oliphant, T. E., et al. 2020, *Nature Methods*, 17, 261
- von Zeipel, H. 1910, *Astronomische Nachrichten*, 183, 345
- Walt, S. v. d., Colbert, S. C., & Varoquaux, G. 2011, *Computing in Science & Engineering*, 13, 22
- Watanabe, N., Narita, N., Palle, E., et al. 2022, *Monthly Notices of the Royal Astronomical Society*, 512, 4404
- Winn, J. N., Fabrycky, D., Albrecht, S., & Johnson, J. A. 2010, *ApJL*, 718, L145
- Winn, J. N., Johnson, J. A., Albrecht, S., et al. 2009, *The Astrophysical Journal*, 703, L99
- Winn, J. N., Howard, A. W., Johnson, J. A., et al. 2011, *The Astronomical Journal*, 141, 63
- Wöllert, M., & Brandner, W. 2015, *A&A*, 579, A129
- Wytttenbach, A., Lovis, C., Ehrenreich, D., et al. 2017, *A&A*, 602, A36
- Yee, S. W., Winn, J. N., Hartman, J. D., et al. 2023, *The Astrophysical Journal Supplement Series*, 265, 1
- Yu, L., Zhou, G., Rodriguez, J. E., et al. 2018, *AJ*, 156, 250
- Zanazzi, J. J., & Lai, D. 2018, *MNRAS*, 477, 5207
- Zhang, Y., Snellen, I. A., Wytttenbach, A., et al. 2022, *Astronomy & Astrophysics*, 666, A47
- Zhang, Z., Bowler, B. P., Dupuy, T. J., et al. 2023, *AJ*, 165, 73
- Zhao, L. L., Kunovac, V., Brewer, J. M., et al. 2023, *Nature Astronomy*, 7, 198